Int J Adv Manuf Technol (2016) 84:1821–1839
DOI 10.1007/s00170-015-7752-4

ORIGINAL ARTICLE

Modeling of friction along the tool-chip interface in Ti6Al4V alloy cutting

Slim Bahi[1] · **Gautier List**[1] · **Guy Sutter**[1]

Received: 11 December 2014 / Accepted: 24 August 2015 / Published online: 22 September 2015

Abstract The aim of the paper is the modeling of chip formation in metal cutting in order to describe the thermomechanical interactions at the tool-chip interface (TCI). A particular attention is paid for the fully sticking case to complete previous modeling works which were more focused on the sliding regime or mixed sliding/sticking regime. The fully sticking contact is dominating due to the combined effects of high magnitudes of the normal stress, the average friction coefficient ($\overline{\mu}\rightarrow 1$) and the temperature. This case is also well adapted for cutting of titanium alloy. In the present model, these local parameters are macroscopically expressed through the average friction coefficient $\overline{\mu}$, and the velocity field on the secondary shear zone is modeled using a new approach. The ratio between real area of contact A_r and the apparent area A_n is taken into consideration. The developed approach is also fully thermomechanically coupled with heat transfer consideration. In this way, it was possible to predict normal and shear stress according to the variation of cutting velocities, feed and rake angle. The model was supported by the experimental trends from Ti6Al4V alloy cutting tests and worn tools analysis. It was shown that the distribution of the ratio A_r/A_n may be considered as a good indicator to describe the spreading of the adhesion marks on the contact. The model also highlights how the influence of the apparent friction coefficient, the rake angle, the feed and the cutting speed acts on the tool-chip contact length.

Keywords Sticking contact · Adhered friction · Titanium alloy machining

✉ Slim Bahi
mohamed-slim.bahi@univ-lorraine.fr

[1] Universite de Lorraine, Metz - cedex 01, Nancy, France

NomenclatureAbbreviations

PSZ Primary shear zone
SSZ Secondary shear zone
TCI Tool–chip interface

Material and tool parameters

σ_{eq} Von Mises equivalent stress (MPa)
ρ Workpiece material density (Kg/m^3)

Cutting conditions

V Cutting speed (m/min)
$t1$ Uncut chip thickness (mm)
α Rake face angle (°)
α_{fl} Flank face angle (°)

Chip characteristics

t_2 Chip thickness (mm)
δ Proportion of the SSZ thickness
R Proportion of the sticking zone interface
ϕ Primary shear angle(°)
τ_0 Shear stress at the entry of the PSZ (MPa)
τ_{PSZ} Shear stress at the exit of the PSZ (MPa)
τ_{st} Shear stress along the sticking zone (MPa)
$\overline{\tau}_{st}$ Average of the shear stress along the sticking zone
σ_0 Normal stress at the tool edge (MPa)
h Primary shear zone thickness (μm)
V_c Bulk chip velocity (m/s)
V Velocity of particle on chip (m/s)

Coefficients

p Decreasing normal stress coefficient
c Coefficient controlling *the shear strain rate*
ξ, ψ, ζ Coefficients of Marinov velocity field

Tool–chip interface parameters

L_c Contact length (mm)
L_s Length of the sticking zone (mm)
L_t Length of the transition zone (mm)
A_r Real contact area (mm^2)
A_n Nominal or apparent contact area (mm^2)

s Stress acting on real contact area (MPa)
$\overline{\mu}$ The average friction coefficient given from the ratio of the cutting forces acting at the TCI
μ_{sl} The sliding friction coefficient

Thermal parameters

k_W, α_W Conductivity and diffusivity of workpiece, respectively (W/m°C)
k_T, α_T Conductivity and diffusivity of tool
C Heat capacity of workpiece material
Q_{SSZ} Heat flux on the SSZ
Q_{sl} Heat flux generated by friction on the sliding zone
T_0 Room temperature (°C)
T_{PSZ} temperature at the exit of the PSZ (°C)
T_t Absolute temperature of tool (°C)
T Absolute temperature of particle on the chip (°C)
R_{ch} Part of heat transmitted to the chip on the sliding zone
$h1$ Coefficient of heat convection, upper side of chip (W/m^2K)
h_{int} Coefficient of conductance at the TCI (W/m^2K)

Forces

F_p, F_q Cutting and feed forces, respectively (N)
F_N, F_f Normal and tangent forces on the rake face, respectively (N)
F_s Shear force on the PSZ (N)
M_{OA} Momentum on tool tip with respect to Fs (N.m)
M_{OB} Momentum on tool tip with respect to FN(N.m)

1 Introduction

Wear and friction remain two main intimately coupled mechanisms that have a direct impact on the quality of the machined workpiece, the cutting tool life duration and the consumed power. The evaluation of boundary conditions at the tool–chip interface (TCI) has become a domain of investigation among the most studied over the last few decades. From an experimental point of view, the common techniques used to analyze the stress distribution at the tool rake are the split tool method [1–3] and photoelasticity [4–6]. For the temperature distribution, several techniques have been used such as infrared or intensified CCD cameras [7, 8], inverse methods with thermocouple placed into the tool [9] and metallographic analysis of chip and worn tools [10]. Based on the analyses of the distribution of stresses and temperature, three contact regimes are usually stated: a perfectly sliding contact [11, 12], an intermediate contact alternating sticking and sliding contact [13] and a fully sticking contact [14]. Please note that these in situ techniques still have an applicability limited to low or moderate cutting speeds, and results cannot be representative for high speed machining. Moreover, experimental data for certain classes of ductile or high strength materials, such as titanium alloy, do not unfortunately exist. The main conclusions given from the various experimental data are usually referred to Zorev [15] or Trent and Wright [16, 17] analyses, suggesting that the interfacial contact occurs along two distinctly regions: (1) a plastic region characterized by a sticking friction with a plastic localization in the secondary shear zone (SSZ) near the tool tip, where stresses reach a maximum level, and (2) an elastic region characterized by a sliding friction and a linear proportionality between normal and shear stresses. In addition, the experimental results show that the friction boundary, i.e. contact length, thickness of plastic deformation zone and the extension of the sticking and sliding zones, is sensitive to the variation of the cutting conditions, the tool and workpiece material properties, the atmosphere and the presence of oxides at the TCI [18]. The adhesion phenomenon may also be affected by the state of magnetization of the tool–chip interface [19]. In other terms, the variation of the energy state of the surfaces in contact leads to modify the atomic bonding between asperities. From a wear point of view, the different damage mechanisms are triggered at each contact regime according to the magnitude of sliding velocity, the pressure level and the temperature rise. Modeling with an accurate depiction of the TCI must be one of primary considerations when tool wear and the surface integrity are major parameters to design cutting tools. The development of numerical means has opened the way for taking into account in friction modeling complex variables such as the temperature effect, mechanical material behavior and the variation of the chip velocity field in the neighborhood of the TCI. In terms of friction, the numerical means allow the modeling of the sticking-sliding contact regime, according to experimental trends and the Zorev's approach [15]. This approach involves that, along the sticking contact, the shear stress τ_{int} is given by the shear flow stress of the chip. In the sliding part of contact, the shear stress τ_{int} is linearly proportional to the normal load σ_n via a sliding friction coefficient $\tau_{int}=\mu_{sl}\cdot\sigma_n$ Indeed, one of the most important boundary conditions, used in numerical models to define the interfacial contact, concerns the definition of the sliding friction coefficient μ_{sl} or the proportion of the sticking part L_s/L_c. This approach implies that the repartition of the contact regimes is directly defined by the two input parameters μ_{sl} and/or τ_{int}. For example, considering μ_{sl} as an input of the numerical model implies indirectly the proportion of the sliding zone with respect to the whole TCI length because it acts on the term of the heat flux generated by friction in this same part of the contact [20]. For better accuracy, the combined effects of the distributions of temperature, strains rates, strains and velocity must be the main parameters controlling the chip flow and the stress repartition on the rake face and, in turn, bring to such or such contact regime, i.e. fully sliding contact, alternating sticking-sliding contact or fully sticking contact.

Today, many numerical simulations of cutting are performed using commercial software. The latter does not always allow the modelling of complex phenomena about the contact as described before. It appears important to continue to develop specific models such as hybrid approaches combining analytical modeling and numerical resolution such as proposed by Marinov [21, 22]. In this work, the concept of the sticking and sliding zones is discussed in light of experimental and modeling approaches during cutting of titanium alloy. The presented model of the TCI is also based on hybrid approach, mixing analytical and numerical means. The foundation of the modelling was initiated by the work of Bahi et al. [23–25], but with thorough changes in the manner of resolving the problem about the switching from sticking and sliding regimes. Contrary to the previous model, the new approach enables the model to approach the cases where high friction coefficients are involved with fully sticking regime along the TCI. The link with the scale of asperities can be now established with the introduction of the notion of the real contact surface area. A particular attention will be attributed to the boundary conditions of the secondary shear zone and their effects on the tribological conditions at the TCI. These boundary conditions are:

- The shape and the velocity field within the secondary shear zone,
- The heat transfer (conductance) at the TCI, and
- the average friction coefficient $\overline{\mu}$, representing the ratio of cutting forces during machining. In macroscopic scale, $\overline{\mu}$ expresses the macroscopic contribution of cutting conditions (cutting speed, feed, rake angle, flank angle). Moreover, this global factor allows the determination of the local contributions of temperature, stresses, strain, strain rates in microscopic scale without imposing μ_{sl} and/or τ_{int}.
- The real contact area A_r spreading with respect to the whole or nominal contact area A_n.
- The workpiece and chip material behavior under effect of shear, shear strain and temperature rise.

The modelling is applied for the case of orthogonal dry machining of the aeronautic titanium alloy with coated and uncoated tools.

2 Contact conditions at the TCI

Before introducing the model (Section 3), the main parameters that control the physics at the tool–chip interface (TCI) are presented including the ratio between the real and nominal surface contact areas. From this analysis, the repartition between sliding and sticking contacts is depicted. A correlation with the experimental observations is done then.

2.1 Contact area and interfacial stress

In cutting process, the high compressive loading at the TCI induces a growth of the contact land with an increase of the shear friction and the feed force. As explained by Bowden and Tabor [26], the seizure contact occurs when the area of true contact approaches the geometric area and this combination is sufficient to cause a plastic flow in the SSZ. A welding solid phase between the primary atomic bonds of clean metallic surfaces is formed, and the chip flow takes place in adjacent layers with the shear velocity gradually increasing until the bulk chip speed is reached. At the same point of view, Wright and Trent [18] have reported this hypothesis specifying that the degree of secondary shear is determined by the character of such bonds and the mechanism by which these can be broken to cause localized sliding in a micro-region. It has been shown that the type of oxide found on the TCI is a major factor in determining the strength of the interfacial bond under extreme shearing. This also means that relative sliding can occur in sticking region when bonds are broken. The seizure can be then qualified as "stick–slip" contact regime.

In this study, a term of "sticking contact" is used for describing fully seizure contact near to the tool tip, with no relative motion on the TCI. The concept of sticking contact is an interpretation offered by Zorev [15] to describe the normal stress and shear stress repartition at the interface based on split tool technique (Fig. 1a). The experiments lead by Childs et al. [2], based on the same technique, demonstrate that on the rake face, the friction stress is not everywhere proportional to the normal stress, especially near to the tool tip. At high normal stress, the friction stress is independent of normal stress, but at low normal stress levels (in the region farthest from the cutting edge), the friction stress becomes proportional to normal stress and the Coulomb friction law can be applied. The main conclusions given by the authors are:

- In the sticking zone, the normal stress σ_n is higher than the shear flow stress acting on the primary shear zone $\sigma_n > \tau_{psz}$. Consequently, the contact is in plastically stressed part of the chip and is established between plastic asperities of the tool and a plastic chip (SSZ). The ratio between apparent area of contact A_r and the whole area A_n is approaching the unity (see Fig. 1b).
- The friction stress τ_{int} capped on the sticking zone is always inferior to τ_{psz}. This is due to the thermal softening effect and presence of solid lubricant phase in workpiece material. In the sliding zone, the shear stress is linearly proportional to the normal stress. Experimental results show that the sliding friction coefficient can be greater than unity $\mu_{sl} = \tau_{int}/\sigma_n \geq 1$. The ratio of the sticking zone depends on three main parameters: the normal load, temperature and thermomechanical characteristics of antagonists (bonds between the asperities). Under sticking friction, at

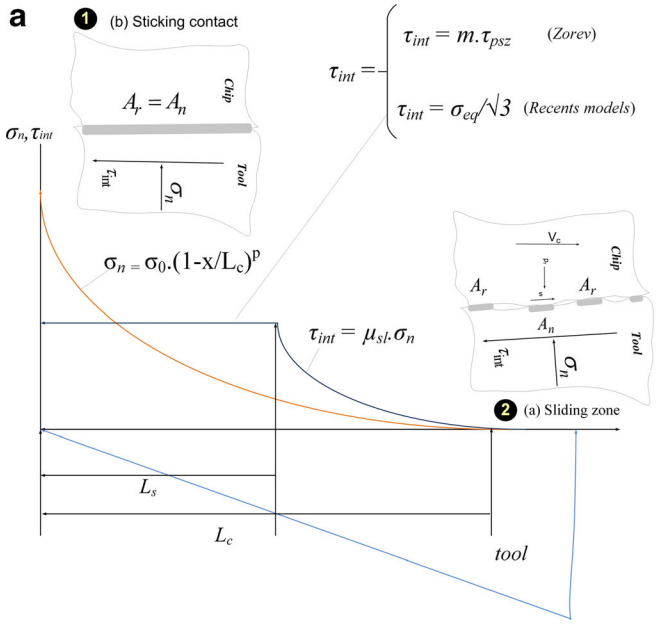

Fig. 1 **a** Normal and shear stresses distribution along the TCI according to Zorev approach [15] and from experimental interpretations [2, 3]. **b** Degree of the contact A_r/A_n is a function of normal load at the TCI [2].

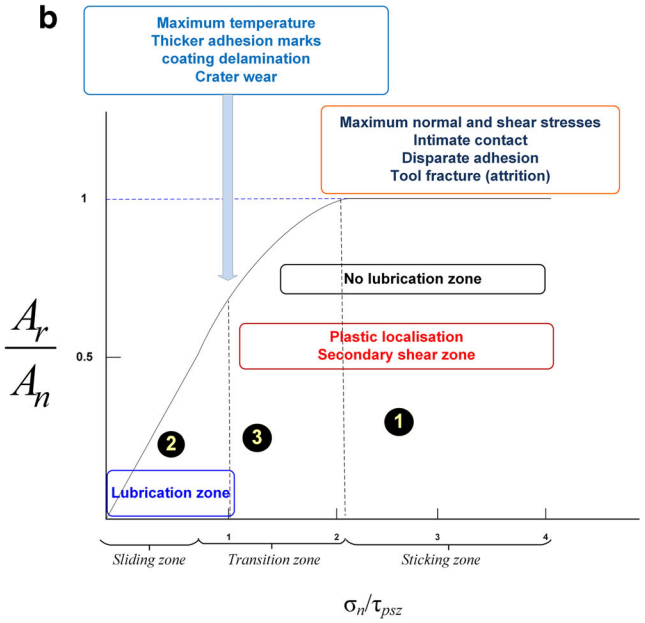

Interpretation of the different contact and wear regimes issued from Childs descriptions of the TCI

speeds greater than tens of m/min for steels, local thermal softening of chip results in a degree of self-lubrication. However, at low cutting speeds, lubricants can penetrate the low stressed contact region (sliding zone).

Figure 1 comes from an interpretation of Childs et al. [27] related to the Zorev's stress distributions at the tool–chip contact. Due to the roughness, the contact may be happen only over a smaller area A_r than the whole contact area A_n. This reduced area transmits the contact forces. Equation (1) gives the relationship between the friction force, the shear stress and the real surface area:

$$F_f = A_r s \tag{1}$$

The strength S of the real contact area A_r is an important parameter which must be more investigated by studying the contact mechanisms of rough surfaces. In addition, friction models must integrate the variability of this strength in the local contact and then enhance a better correlation between wear and friction mechanisms. This is the subject of a future investigation in order to improve the friction model presented in the next section. Recent investigations led by Gerth et al. [28] confirm this point of view. It was shown that the tool surface topography and chemistry on the adhesion phenomena in the SSZ have a profound effect on the ratio of the sticking and the sliding zones and consequently on the wear mode. This topic will be discussed in the next section.

The interfacial friction stress is given by:

$$\tau_{\text{int}} = \frac{F_f}{A_n} = \frac{A_r}{A_n}.S \tag{2}$$

Childs [29] improved his friction contact model by an empirical relation, proposed by Finnie and Shaw [30], relating the A_r to A_n expressed as:

$$A_r = A_n\left(1-e^{-B\sigma_n}\right) \tag{3}$$

Combining $\tau_{\text{int}} \infty A_r$ with Eq. (2) and substituting $\tau_{\text{int}} = \sigma_{\text{eq}}/\sqrt{3}$ (shear flow stress of chip) when $A_r = A_n$ and $\tau_{\text{int}} = \mu_{\text{sl}} \cdot \sigma_n$ when $A_r \ll A_n$ (then $(1-e^{-B\sigma_n}) \approx B\sigma_n$) leads to Eq. (4), with $\mu_{\text{sl}} \sqrt{3}/\sigma_{\text{eq}}$ identified as B:

$$\tau_{\text{int}} = \frac{\sigma_{\text{eq}}}{\sqrt{3}} \cdot \left(1-e^{-\mu_{\text{sl}} \cdot \sigma_n \cdot \sqrt{3}/\sigma_{\text{eq}}}\right) \tag{4}$$

Equation (4) expresses the local friction stress as function of the local chip material flow stress $\sigma_{\text{eq}}/\sqrt{3}(T, \gamma, \dot{\gamma})$ and the local normal stress. This implies that μ_{sl} cannot be constant over the whole of TCI. At low contact stresses, it reduces $(A_r/A_n) = B.\ \sigma_n$. As a limit of this Eq. (4), Childs concludes to the need of integrating a better formulation regarding the ratio A_r/A_n, its dependency on the normal load σ_n and the plastic deformation at the SSZ. Moreover, the sliding friction coefficient μ_{sl} must express a sensibility to the SSZ and the parameter B, which can

represent a term related to the adhesion rate in the sliding zone and the strength s of the asperities on the contact.

2.2 Sticking and sliding contact

SSZ can play lubricant role when sticking dominant. Experimental investigations show that at high speed machining, around 50 m/s, the average friction coefficient $\overline{\mu} = F_f/F_n$ is decreasing dramatically due to the thermal softening effect [31, 32]. For example, in the case of medium carbon steel, at V=50 m/s, t_1=0.5 mm, $\overline{\mu} = F_f/F_n = 0.2$, the level of mean friction coefficient, given from the experimental ratio of cutting forces, is similar to those under zero charge loading. This can be explained by the formation of a "transition flowing zone" at the TCI, within the SSZ, having a behavior similar to fluid lubricant layer. In the position where the shear strain rate $\dot{\gamma}$ of the chip reaches a maximum, the flow of the chip operates at some distance from the real TCI. At high speed machining conditions, the different tribological parameters reach a maximum level, $\dot{\gamma} = 10^8 s^{-1}$, $T \approx T_f$ $\sigma_n \geq 3GPa$, and the fall of global friction coefficient is a consequence of the formation of a transition flowing layer between tool–chip junctions of the asperities and within the chip (similar to the third body). To describe this zone, Qi and Mills [33] proposed a realistic velocity distribution at the boundary of the tool–chip interface, where the material has a complex mixed composition between tool and workpiece material with a transition flowing zone. The hybrid model presented in this work integrates a similar velocity profile.

The frictional boundary is expressed by an instantaneous variation (over the start of engagement within the interfacial contact) of an extent and geometry of sticking and sliding interfaces due to variation of tribological parameters inside the SSZ and the variation to the TCI bonding due to the wear mechanisms. In the works of M'Saoubi et al. [34], the coupled analysis of temperature distribution and SEM-EDS element mapping of tool rake surface enabled authors to distinguish three different regions in contact: sticking contact followed by a transition zone and, at the exit of contact, a region subject of thicker adhesion marks defined by the authors as the sliding zone. Recently, Wiklund et al. [35] have used different microscopic techniques, such as transmission electron microscopy, X-ray photoelectron spectroscopy and scanning electron microscopy to study the adhesion phenomena when cutting stainless steel. The authors reported also three different zones of the contact; the first one is the fractured region with adhered contact between the chip and the tool. In the second region, the tool–chip contact is intimate and a stagnant layer is likely to be developed; this layer is only located at the areas free of indents and could reveal the mechanism of adhesion. Finally, in the third region, farthest from the tool edge, the contact is made temporally between the chip and the tool, leaving remnants of work material adhered. The authors noted that the adhesion between this material and the chip is higher than the cohesion in the chip at the time of such contact. In recent research, Gerth et al. [28] have observed the contact area between chip and the rake face, and they suggested dividing this area into three different regions based on differences in surface appearance, material transfer and cutting conditions. This classification is also suggested by Wiklund et al. [35]. The first area adjacent to the cutting edge is characterized by high normal stresses, the second region is an area about 300 μm from the tool tip where temperature during cutting reaches a maximum and finally and the third region is an area where the chip separated from the rake face and plenty of oxygen is present in contact during cutting.

2.3 Correlations with experimental results

In this study, orthogonal cutting tests have been used on the Ti6A14V titanium alloy workpiece and a TiA1N-coated cemented carbide tool. The machining conditions are given in Table 1, and some results were already presented in [23–25]. The resultant force in cutting (F_p) and feed direction (F_q)were measured using a Kistler dynamometer.

Figure 2a represents a micrograph of the Ti6Al4V workpiece structure before machining which has a duplex structure $\alpha/\alpha+\beta$, with average grain size (for both α and β grains) around 10 μm (range from 5 to 20 μm) and average microhardness $320HV_{0.2}$. The substrate of the cutting tool is made of tungsten carbide (WC) with 6 % cobalt (Co), and all inserts had an applied single layer of TiA1N coating with average thickness of 4 μm.

In Fig. 2b–d, the micrograph of the Ti6Al4V chip shows two distinct zones; the first zone presents a transition flowing zone with beta grains deformed in the direction parallel to the rake face due to the high compressive load on the TCI (blue lines). In the second zone, at some thickness from the TCI, the orientation of the deformed grains is more different and testifies to a reduced influence of normal load. The velocity gradient in the chip can be deduced from the orientation of deformed grains, with maximum strain rate near to the rake face

Table 1 Machining conditions used in the experiment

Machining setup	Dry orthogonal cutting
Total cutting length	L=12 mm interrupted every 4 mm
Tool material	WC-Co and WC-Co coated TiAlN
Tool geometry	Rake angle α: 5°, 15°, 20° and 30°
Flanck angle α_{fl}: 7°	
Feed	f=0.12 mm and 0.2 mm
Cutting speed	V=15,30 and 60 m/min

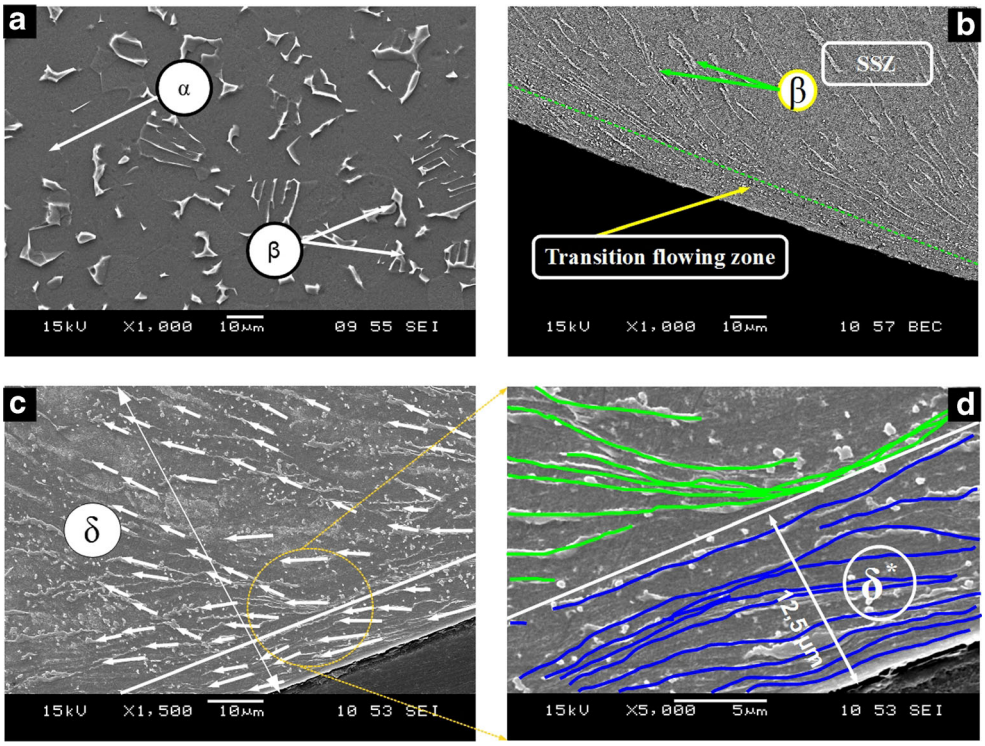

Fig. 2 **a** Microstructure of Ti6Al4V alloy before machining, **b** microstructure of Ti6Al4V chip with zoom on the SSZ, **c** orientation of the deformed grains in the SSZ thickness and close to TCI. **d** Zoom of the transition flowing zone thickness considered as a part of SSZ submitted to high compressive load [23]

and decreasing within the chip thickness, as suggested by the modeled velocity fields presented in the next section.

Figures 3 and 4 show the evolution of the tool–chip contact length and the different wear mechanisms observed on the tool rake face. These mechanisms are principally adhesion of titanium and abrasion, and for feed f=0.2 mm the fracture of the tool-tip. From the micrographs, it is easy to remark that the contact area between chip and rake face shows two distinct zones. The region close to the tool tip, noted (Z1) in Fig. 3, is subjected to thin and disparate adhesion marks on the interface, especially at low speed 15 m/min. However, these marks become thicker and uniform in the region (Z2) and the rate of titanium adhesion on the rake face grows considerably with cutting speed. As shown in Fig. 3b, the rate of adhesion is localized intensively on the irregularities of the rake face, which means that contact is intermittent in this zone and then favors the presence of oxygen and the formation of adhesion deposit. The chip and the tool are in such frictional contact that the ratio between the real and apparent areas of contact is less than unity but sufficiently higher to lead to a plastic deformation within the chip. Under this condition, this region is considered typically characterized by stick–slip contact, i.e. a combination of frictional and sticking contact with plastic deformation can exist.

With the increase of the cutting speed, a third zone (Z3) appears at the end of the contact and presents thicker and non-uniform adhesion marks. An interesting similarity is observed between wear mode and the concentration of adhesion on this zone (Z3) and those observed on the flank face (not presented in this paper),

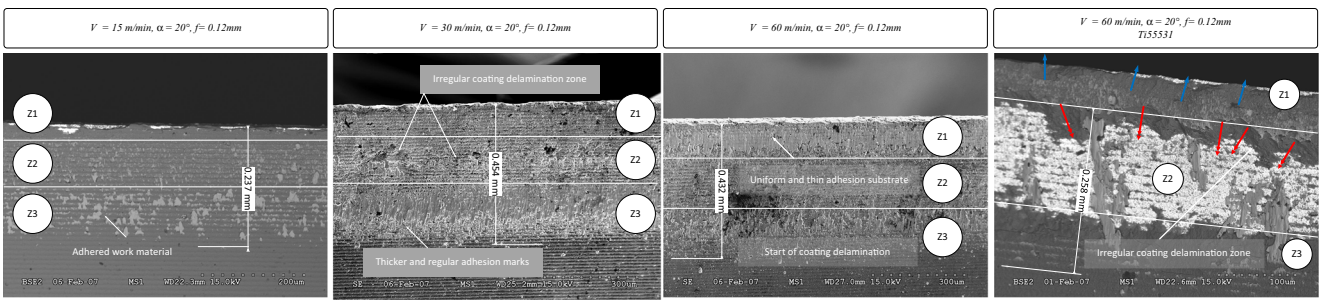

Fig. 3 Effect of the cutting speed V, analysis of wear modes on tool rake face, estimation of the total contact length and identification of different wear zones based on appearance of the adhered material deposit marks. *Z1*: zone with thin and disparate adhesion marks, *Z2*: zone with thin or moderate adhesion marks and start of coating delamination mode and *Z3*: zone with thicker and regular adhesion marks located on the exit of the chip. Cutting conditions from the *left* (Micrographs published on [23–25])

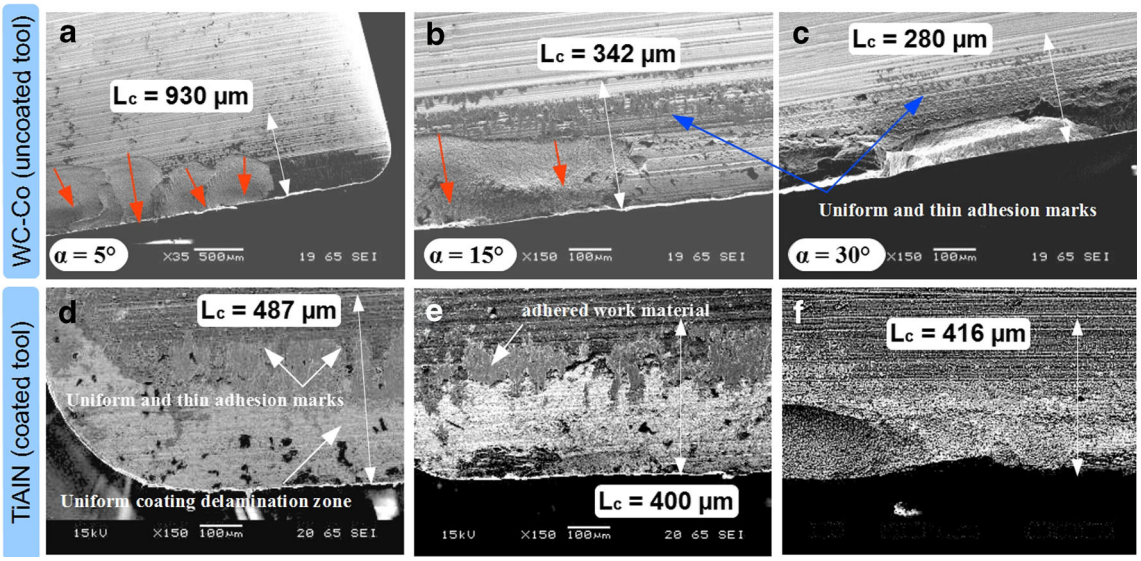

Fig. 4 Effect of coating and rake face angle α. Analysis of wear modes. notching and fracture of the tool tip and small adhesion on the exit region of chip in the case of uncoated tools (**a**), (**b**) and (**c**). Important adhesion and coating delamination wear in the case of TiAlN-coated tool, plastic deformation of the tool and fracture of the tool-tip when α increases (**e**, **f**). The cutting conditions V=60 m/min., f=0.2 mm

which is known as perfectly sliding area. The thickness augmentation of the adhesion deposit is caused by the abundance of the oxygen element at the TCI due to the reduced ratio A_r/A_n (tends to 0). Inversely, in the first region of tool–chip contact, the compressive stresses prevent relative motion at the interface. Under the feed force, a relative motion occurs within the chip and leads to the thermoplastic shear localization in the called secondary shear zone (see Fig. 2b–d). The marks of adhesion are very thin and uniform caused by the compressive loading leading to a ratio A_r/A_n tending to the unity (see Fig. 3).

At 60 m/min, slight and uniform adhesion marks are observed in zone 1, suggesting to be a part of the transition flowing zone (see Fig. 3). When cutting the hard material Ti 5553 at the same conditions, slight adhesion marks are also observed in zone (Z1) with a fracture of the coating material close to the cutting edge. The direction of the coating fracture shown by red arrows close to the tool tip is opposite to the fracture direction in zones (Z2) and (Z3). Here, the mechanism of abrasion dominates due to the destruction of bonds between asperities and the movement of new hard particles (third body). The abrasive wear mode is accelerated when high cutting temperatures, generally above 1000 °C, tend to modify the properties of the coating material by weakening the cobalt binder into the tool.

In Fig. 4, the undeformed chip thickness have been increased (f=0.2 mm) which implies high stresses operating to remove the material on the cutting surface. The main wear mechanism observed in the case of WC-Co tool is the notching and fracture of the tool tip, which reveals a combination of high temperature and stresses. However, the adhesion wear is more important in the case of TiAlN-coated tools, which can be explained by the chemical affinity between the coating material and workpiece. In addition, the reduced thermal conductivity of the coating confers to the TiAlN a role of a thermal barrier which preserves the strength of the cobalt binder in the substrate of the tool and then reduces the fracture mechanism and the temperature of the TCI.

The effect of the increase of the rake angle α reduces the tool–chip contact length and the area affected by the damage of the tool substrate (uncoated tool, Fig. 4a–c) and by coating delamination (coated tool, Fig. 4e–d). However, the failure of the tool edge is more important when rake angle increases due to the decrease of the TCI temperature which limits the thermal softening of the workpiece material and then maintains high shear stresses in contact.

To conclude, four types of wear mechanisms are identified. In zone Z1, close to the tool tip, when the normal load is in maximum, sticking tendencies with very small adhesion rate are triggered when temperature is moderate (800 °C for Ti6Al4V alloy). When temperature of TCI is important, sticking tendencies with melt wear (thin adhesion marks) are triggered in zone Z1. The combination of high normal load and high temperature can lead to plasticity-dominated wear. In zones Z2 and Z3, the decrease of the ratio $\frac{A_r}{A_n}$ with the normal load and the growth of the temperature favorites the presence of oxygen atoms in a vacuum presents in TCI and then leads to an oxidation-dominated wear and thicker adhesion marks. These tendencies will be confronted with numerical results given by the following hybrid model.

3 Hybrid modeling of the contact of the tool–chip interface

3.1 Velocities field and strain rates in the SSZ

In this proposed model, two velocity distributions can be used. The first one is the more simplified model inspired by the work of Oxley [14, 36], Fig. 5a). The SSZ is assumed to be similar to a thin band, and the shear strain rate is constant within the shear zone thickness. However, this velocity field is overestimating and does not permit to find the non-linear increasing of the shear strain rate observed experimentally and depending on position along the rake face [23].

The second velocity model, based on Marinov's work [21, 22], is more realistic and reproduces quite well the experimental result of Bao and Stevenson [37] along the length of the sticking zone L_s (see Fig. 5b). The bulk chip velocity, Eq. (5), is obtained from the material conservation principle ($V{\cdot}t_1{=}V_c{\cdot}t_2$) and geometrical projection (see Fig. 6):

$$V_c = V{\cdot}\frac{\sin\phi}{\cos(\phi-\alpha)} \tag{5}$$

with

$$t_2 = t_1\frac{\sin\phi}{\cos(\phi-\alpha)} \tag{6}$$

The distribution of the material particle velocity V_x in the chip is inspired by work of Oxley [14] (model 1), Eq. 7(a), Fig. 5a) and Marinov [21] (model 2), Eq. 7(b)), Fig. 5b).

Velocity distribution, Model 1	Velocity distribution, Model 2
Velocity	***Velocity***
$V(x,y)=\begin{cases} V_c{\cdot}\frac{y}{\delta} & if \begin{cases}0\le x\le L_s\\ y\le\tilde{\delta}(x)\end{cases}\\ V_c\left(\frac{x-L_s}{L_t}+\frac{y}{\delta}\right) & if \begin{cases}L_s\le x\le L_s+L_t\\ y\le\tilde{\delta}(x)\end{cases}\\ V_c & if\ L_s+L_t\le x\le L_c\end{cases}$ (7a)	$V(x,y)=V_c(\xi-\xi\psi+\psi)^c$ (7b)
The thickness $\tilde{\delta}$ of the secondary shear zone is decreasing linearilly along the transition zone, Eq. (8a):	with $\psi=\frac{y}{\delta(1-\zeta)},\quad \zeta=\frac{x}{L_s+L_t}$
$\tilde{\delta}(x,y)=\begin{cases}\delta & if\ 0\le x\le L_s\\ \delta\left(1-\frac{x-L_s}{L_t}\right)\end{cases}$ (8a)	$\xi=\begin{cases}0 & \text{if } 0\le x\le L_s\\ \frac{x}{L_s+L_t} & \text{if } L_s\le x\le L_s+L_t\\ 1 & \text{if } L_s+L_t\le x\le L_c\end{cases}$ (8b)
Shear strain rate	***Shear strain rate***
$\dot{\gamma}(x,y)=\frac{dV}{dy}=\frac{V_c}{\tilde{\delta}}$ (9a)	$\dot{\gamma}(x,y)=\frac{dV}{dy}=\begin{cases}V_c.c.\left(\frac{V}{V_c}\right)^{\frac{c-1}{c}}\frac{1}{\delta(1-\zeta)}\\ V_c.c.\left(\frac{V}{V_c}\right)^{\frac{c-1}{c}}\frac{1}{\delta}\\ 0\end{cases}$ (9b)

3.2 Boundary conditions of the primary shear zone

The details of the primary shear zone model are presented in previous works and based on the approaches developed by Dudzinski and Molinari [38]. This zone is assumed to be a thin band layer with a uniform thickness h and to be oriented by an inclination angle ϕ to the direction of the cutting speed (Fig. 6). The boundary conditions of the PSZ are illustrated in Fig. 7. The modified Johnson-Cook's law [24, 39] presented in Eq. (10)

is used to describe the shear flow into the SSZ. This formulation takes better into account the hardening sensitivity at high shear strain rate (Eqs. (9A) and (9B)) through an identified critical strain rate $\dot{\gamma}_t$:

$$\tau_{st} = \begin{cases} \frac{1}{\sqrt{3}}\left[A + B\left(\frac{\gamma}{\sqrt{3}}\right)^n\right] \left[1 + m\, ln\left(\frac{\dot{\gamma}}{\dot{\gamma}_0}\right)\right] \left[1 - \left(\frac{T - T_r}{T_m - T_r}\right)^{\nu}\right] & if \quad \dot{\gamma} \le \dot{\gamma}_t \\ \frac{1}{\sqrt{3}}\left[A + B_2\left(\frac{\gamma}{\sqrt{3}}\right)^n\right]\left[1 + ln\left(\left(\frac{\dot{\gamma}}{\dot{\gamma}_0}\right)^{m^*}\left(\frac{\dot{\gamma}_t}{\dot{\gamma}_0}\right)^{m-m^*}\right)\right]\left[1 - \left(\frac{T - T_r}{T_m - T_r}\right)^{\nu}\right] & if \quad \dot{\gamma} > \dot{\gamma}_t \end{cases} \tag{10}$$

A and B are workpiece material parameters, the coefficients n, m and ν are the strain sensitivity coefficient, the strain rate sensitivity and the thermal softening coefficients, respectively. m^* and B_2 are the strain rate sensitivity coefficient and the parameter which controls the level of strain hardening at dynamic

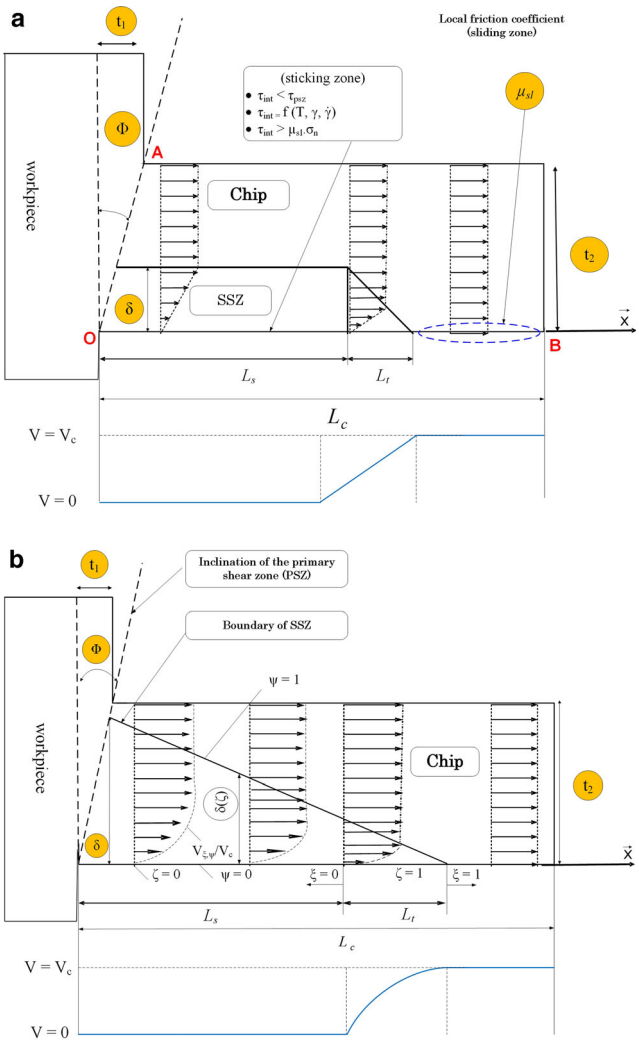

Fig. 5 Velocity profiles in the plastic deformation zone, shape and dimensions of the secondary shear zone. **a** After Bahi et al. [24] and inspired by work of Oxley. **b** After Marinov [21]

domain, respectively. In the PSZ, the shear stress τ_{PSZ}, the absolute temperature T and the shear strain rate $\dot{\gamma}$ are obtained from constitutive law and the integration of the equations of motion and heat (assuming adiabatic conditions) and the development of these distributions is detailed on [38] and [40]. The shear stress at the exit of the primary shear zone is expressed by Eq. (11):

$$\tau_{PSZ} = \rho \cdot (V \cdot \sin\phi)^2 \cdot \gamma_h + \tau_0 \tag{11}$$

with $\gamma_h = \frac{\cos\alpha}{\sin\phi\cos(\phi - \alpha)}$ the saturated strain at the exit of the PSZ and τ_0 the shear stress at the entry of the PSZ. The details of the calculation of τ_0 are explained in [24].

For the temperature of outflow of the PSZ we have:

$$T_{PSZ} = \frac{\beta}{\rho c}\left(\rho \cdot (V \cdot \sin\phi)^2 \cdot \frac{\gamma_h^2}{2} + \tau_0 \cdot \gamma_h\right) + T_w \tag{12}$$

The shear force acting on the PSZ is given by:

$$F_s = \tau_{psz} \frac{w \cdot t_1}{\sin\phi} \tag{13}$$

3.3 Boundary conditions of the secondary shear zone and the tool–chip interface

The geometrical shape of the chip and the secondary shear zone, the thermal boundaries conditions and the distribution of the velocity field along the TCI are illustrated in Fig. 8.

As explained previously, the contact ratio as proposed by Childs et al. is proportional to the normal stress as follow:

$$A_r = A_n \cdot \left(1 - e^{-B \cdot \sigma_n}\right) \tag{14}$$

To simplify the problem, the decreasing form relating A_r to A_n with absolute position on the TCI is expressed as follow:

$$dA_r = \left(1 - \frac{x}{L_c}\right)^p dA_n \tag{15}$$

with $p \in IR^+$ and $A_n = w\, L_c$.

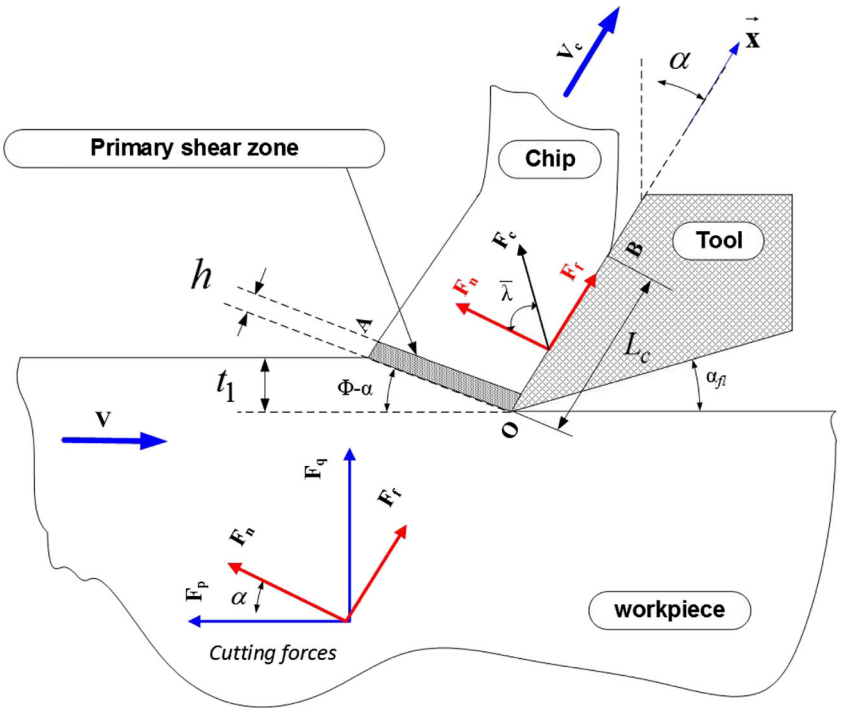

Fig. 6 Geometrical characteristics of the primary shear zone PSZ and of the chip

Then, as the normal force is the sum of the normal stresses acting on asperities loaded (A_r), the normal force, decomposed along the rake face, is expressed as follow:

$$F_n = \iint_{A_r} \sigma_r \, dA_r = \iint_{A_n} \sigma_0 \left(1 - \frac{x}{L_c}\right)^p dA_n \quad \text{with} \quad dA_n = dx{\cdot}dz \tag{16}$$

$$F_n = \sigma_0{\cdot}w \int_0^{L_c} \left(1 - \frac{x}{L_c}\right)^p dx = \frac{w{\cdot}\sigma_0{\cdot}L_c}{(p+1)} \tag{17}$$

From the momentum equilibrium M_{OA}=M_{OB} (Fig. 6), using Eqs. (13) and (17), the normal stress acting on the tool tip σ_0 and the tool–chip contact length L_c are obtained:

$$\sigma_0 = 4.\tau_{\text{psz}} \frac{(p+1)}{(p+2)} \cdot \frac{\cos^2\lambda}{\sin(2(\phi + \lambda - \alpha))} \tag{18}$$

$$L_c. = \frac{t_1}{2\sin\phi} \frac{\sin(\phi + \lambda - \alpha)}{\cos\lambda} .(p+2) \tag{19}$$

The global friction coefficient is a macroscopic parameter, representing the response of combined local effects of temperature, stresses and strain rates;

$$\overline{\mu} = \frac{F_p \, tg\,\alpha + F_q}{F_p - F_q \, tg\,\alpha} \tag{20}$$

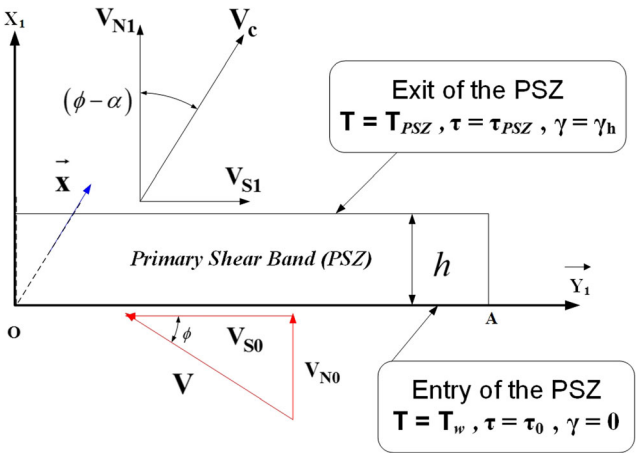

Fig. 7 Boundary conditions of the PSZ

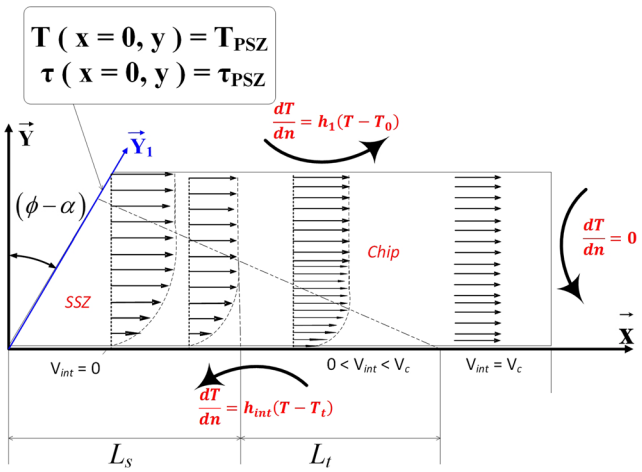

Fig. 8 Boundary conditions of the chip and SSZ

Taking into account the sticking contact regime, the forces acting on the TCI can be decomposed as:

$$\overline{\mu} = \frac{F_f}{F_N} = \frac{w.\int_0^{L_s+L_t} \tau_{st}\, dx + w.\mu_{sl}\,\sigma_0 \int_{L_s+L_t}^{L_c} \left(1-\frac{x}{L_c}\right)^p dx}{w.\sigma_0 \int_0^{L_c} \left(1-\frac{x}{L_c}\right)^p dx} \quad (21)$$

The continuity relation of the shear stress at the TCI is satisfied by neglecting the sliding friction along the transition zone:

If $x=L_s+L_t$ then

$$\mu_{sl}.\sigma_0 \left(1-\frac{L_s+L_t}{L_c}\right)^p = \tau_{(L_s+L_t,0)}\left(T,\gamma,\dot{\gamma}\right) \quad (22)$$

Combining Eqs. (18), (19), (21) and (22), the sliding friction coefficient is calculated:

$$\mu_{sl} = \overline{\mu}/(1-R)^p \left[\frac{\overline{\tau}_{st}}{\tau_{(L_s+L_t,0)}}.R.(p+1) + (1-R)\right] \quad (23)$$

The ratio $R = \frac{L_s+L_t}{L_c}$ is obtained when solving the non linear thermomechanical problem of the chip and by verifying this implicit relation:

$$\mu_{sl}\frac{\sigma_0}{\tau_{(L_s+L_t,0)}}\left(1-\frac{L_s+L_t}{L_c}\right)^p - 1 = 0 \quad (24)$$

In the case of perfectly sliding contact $R=0$, the local friction $\mu_{sl} = \overline{\mu}$, Eq. (23) and $\tau_{int}=\mu_{sl}.\sigma_n$.

Note that the sliding friction coefficient μ_{sl} in Eq. (23) is a function of the global or macroscopic coefficient $\overline{\mu}$, the length of the sticking zone via the ratio R and the ratio $\overline{\tau}_{st}/\tau_{(L_s+L_t,0)}$, characterizing the plastic deformation in the SSZ. In interesting dependency on the spreading of pressure and real contact area, characterized by the coefficient p, is also present. In the cases of perfectly sliding or sliding-sticking contact regimes, R and μ_{sl} are calculated for a given coefficient p, considered as an input parameter.

3.4 Case of fully sticking contact

In the case of fully sticking contact, for $R=(L_s+L_t)/L_c=1$, μ_{sl} is finite and the global friction coefficient $\overline{\mu}$, Eq. (21), is expressed as follow:

$$\overline{\mu} = \frac{F_f}{F_N} = \frac{w.\int_0^{L_c} \tau_{st}.dx}{w.\sigma_0 \int_0^{L_c} \left(1-\frac{x}{L_c}\right)^p .dx} \quad (25)$$

then

$$\overline{\mu} = \frac{\overline{\tau}_{st}}{\sigma_0}(p+1) \quad (26)$$

Contrary to the case of contact regimes presented previously, the parameter p can be obtained by combining Eq. (18), Eq. (19) and Eq. (25) and by solving this resulting implicit equation:

$$(p+2) - 4\frac{\sin\lambda.\cos\lambda}{\sin(2(\phi+\lambda-\alpha))}\,\frac{\tau_{\mathrm{psz}}}{\overline{\tau}_{\mathrm{int}}(T,\gamma,\dot{\gamma})} = 0 \quad (27)$$

Remind that the parameter p controls two coupled parameters: (i) the decrease of the contact lands along the TCI expressed by the ratio A_r/A_n and (ii) the decrease of the normal stress along the TCI. The coefficient p is related to the macroscopic friction coefficient $\overline{\mu} = tan^{-1}(\lambda)$, to the shear flow stress at the PSZ τ_{psz}, to the shear angle ϕ, to the rake face angle α and also to the workpiece material flow via the shear stress τ_{st}.

Equation (25) shows an interesting construction of the average friction coefficient $\overline{\mu}$, which in fact represents a average of a non linear adhesion coefficient along the interface:

$$\overline{\mu} = \frac{1}{n+1}\sum_{i=1}^{i=n+1} \mu_{\mathrm{adh}i} = \frac{(p+1)}{(n+1).\sigma_0}\sum_{i=1}^{i=n+1} \tau_{st}\,(x_i, y_i = 0). \quad (28)$$

n is a number of contacting points between asperities on the interface.

Finally, when adhered friction dominates with sticking contact regime on the whole of the TCI, the friction stress is independent from the normal one, then the local ratio μ_{adh} is non-linear (Eq. (28) and Fig. 9a). However, when the sliding friction mode dominates, the ratio μ_{sl} between local stresses becomes constant (Eq. (23), Fig. 9b).

In the work of Lim and Ashby [41], the authors pointed out that the increase of the number n of contacting points is a result of the growth of the normal load, and not inducing a growth of the average real contact area A_r of an asperity (*size*) as proposed by others authors (e.g. Bowden and Tabor [26]). The authors also explain that when the load is light, the number n must be small ($n\geq 1$). At the extreme load, when load approaches the seizure load, the "unit" contacts overlap and the true number of contacts again becomes small: In the limit of complete seizure, it again goes to 1. In other terms, the contact is constructed as a "single" asperity. In future work, a particular attention must be paid to determine n.

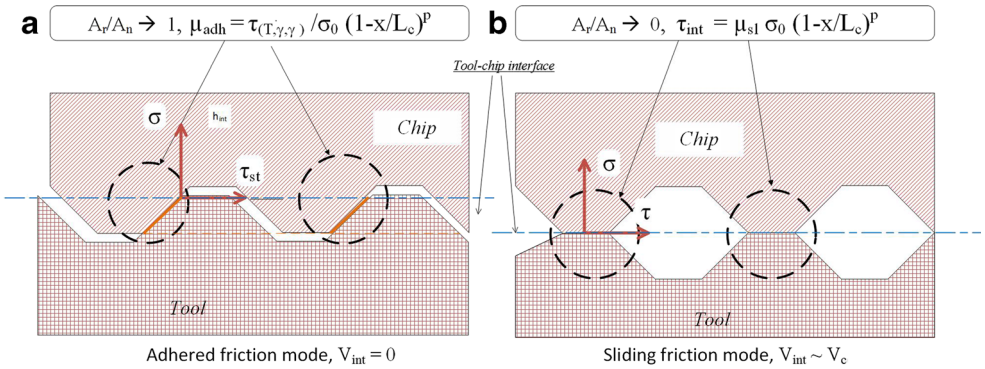

Fig. 9 **a** The adhered friction mode, constant. **b** The sliding friction mode, constant

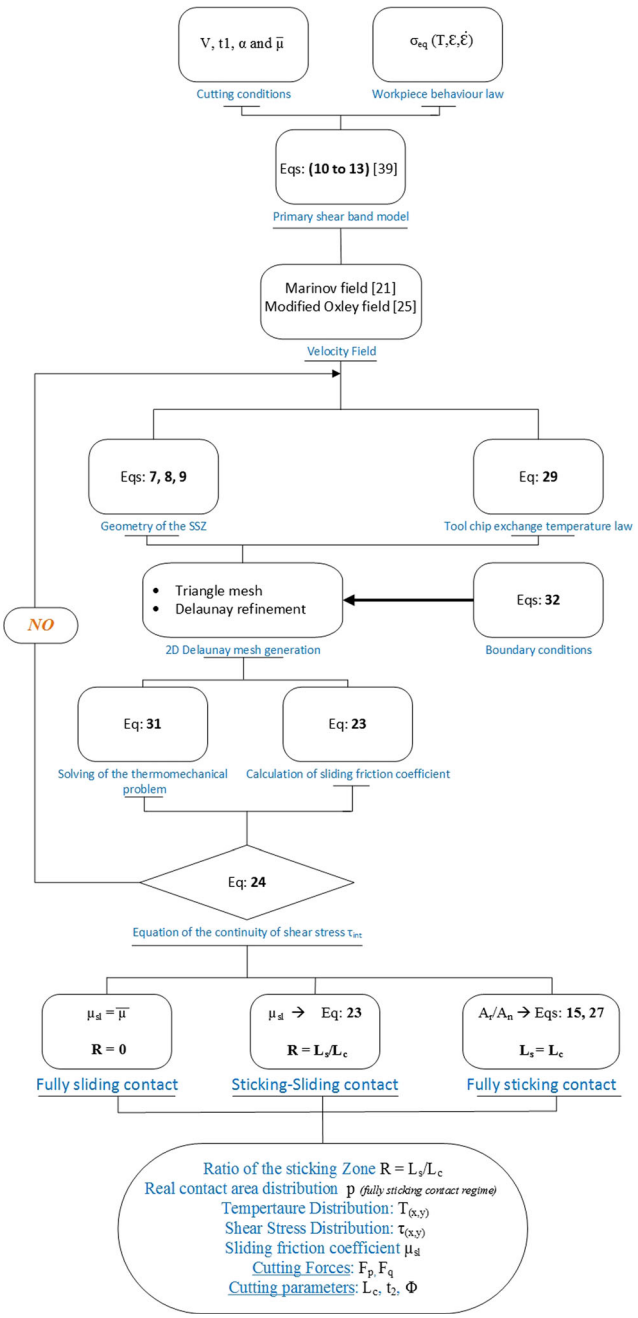

Fig. 10 Diagram of the proposed hybrid approach

3.5 Heat generation in the secondary shear zone and on the tool–chip interface

At the TCI, the heat flux is a result of plastic deformation in the SSZ along the sticking zone and by friction between asperities along the sliding zone. In this model, the heat flux generated by friction along the transition zone is neglected and only considered given by plastic deformation process.

In the sliding zone, the heat transmission coefficient R_{ch}, defining the percentage of the heat entering the chip, is choosing according to the work of Grzesik and Nieslony [42].

$$R_{ch} = \frac{1}{1 + \frac{3}{2}\left(k_T/k_W\right)\left(\sqrt{\alpha_W/\alpha_T}\right)} \tag{29}$$

Taking account the sticking and sliding contact regimes, the heat flux generated on the TCI is given by:

$$Q(x,y) = \begin{cases} Q_{ssz}(x \le L_s + L_t, y) = \dfrac{\sigma_{eq}(x,y)}{\sqrt{3}}\ \dot{\gamma}\,(x,y) \quad \text{with} \quad \dot{\gamma}\,(x,y) = dV(x,y)/dy \\ Q_{sl}(L_s + L_t < x \le L_c, 0) \quad = \quad \mu_{sl} \cdot\ R_{ch} \cdot\ \sigma_0 \left(1 - \dfrac{x}{L_c}\right)^p \ \cdot\ V_C \end{cases} \tag{30}$$

The temperature distribution in the chip is obtained by solving numerically the following 2D heat equation in the steady state:

$$k(T) \cdot \Delta T + Q_{SSZ} = \rho C\, V_x(x,y)\, \frac{\partial T}{\partial x} \tag{31}$$

with respect to the boundary conditions as shown in Fig. 8:

$$\begin{cases} \vec{y}.\ \left(\overrightarrow{k\ grad T}\right) \quad = \quad h_1(T - T_0) & in\ \partial\Omega_{conv} \\ \vec{x}.\ \quad \left(\overrightarrow{k\ grad T}\right) \quad = \quad 0 & in\ \partial\ \Omega_1 \\ -\vec{y}.\left(\overrightarrow{k\ grad T}\right) = h_{int}(T - T_t) + R_{ch}.Q_{sl} & in\ \partial\ \Omega_{int} \\ T_{(x=0\ ,\ \ y)} = \quad T_{PSZ} & in\ \partial\Omega_{PSZ} \end{cases} \tag{32}$$

The diagram in Fig. 10 summarizes the different steps performed on this model.

Table 2 Material parameters of the modified Johnson-Cook law for the Ti6Al4V alloy [24]

A(MPa)	B(MPa)	B_2(MPa)	m	m^*	n	v	T_m	$\dot{\gamma}_t$ (s^{-1})
862	331	314.38	0.012	0.1302	0.34	1	1658	$3.\ 10^3$

4 Results

In this section, the hybrid model is used to determine: (i) global parameters such as cutting forces, contact length and chip thickness and (ii) local parameters at the TCI such as the ratio of the sticking–sliding zones, temperature, the normal and shear stress distributions.

4.1 The simulations step for dry cutting Ti6Al4V alloy

4.1.1 Workpiece behavior and material parameters

The Johnson Cook parameters used for Eq. (10) are given in Table 2. The material conductivity for workpiece depends on the temperature and described using the following equation [43]:

$$k_W = -0.23 + 1.46\ 10^{-2}\ T \tag{33}$$

The natural heat convection coefficient is chosen as $h_1 = 17\ W/m^2K$.

In the case of uncoated tool, the conductance at the TCI, Eq. (32), is chosen $h_{int}=10^3\ W/m^2K$. However, in the case of TiAlN-coated tools, the presence of Ti element on the coating substrate can be considered as a contributing factor of chemical affinity which may increase the phenomenon of adhesion. Therefore, the conductance may be chosen greater than uncoated tools. In this work, the conductance, for the considered coated tools, is chosen one hundred times greater than uncoated tools $h_{int}=10^5\ W/m^2K$.

4.1.2 Geometrical parameters

The velocity field is modeled according to the approach of Marinov described by Eq. 7(b), with the parameter c at 0.25. According to the experimental observations in Section 2.3, the secondary shear zone and the primary shear band thicknesses are respectively estimated as $\delta=0.1t_2$ and $h=25\ \mu m$.

The primary shear angle ϕ is given by Zvorykin's law [44]:

$$\phi = A_1 + A_2\left(\alpha - \overline{\lambda}\right) \tag{34}$$

with $A_1 = 45°; A_2 = \frac{1}{2}$;

4.1.3 The model inputs parameters

The inputs parameters of the model are explicitly the mean friction factor $\overline{\mu}$, the cutting velocity V, the cutting feed f and the rake angle α. In a first step, the thermomechanical problem is solved in the primary shear zone (PSZ) where the normal stress at the tool tip and the chip temperature at the entry of the PSZ are determined. Then, the next step in the model is dedicated to predict the contact regimes, the stress distribution and the temperature among the TCI (see diagram in Fig. 10). The velocity field controls the shear strain rate $\dot{\gamma}$ at the SSZ, and an approximation of the ratio L_s/L_c are introduced to initialize the solving of the thermal equation (Eq. (31)) and the mechanical part of the problem (Eq. (24)). This enables to know the state of the contact: perfectly sliding, sticking-sliding or perfectly sticking. The last case suggests the calculation of the coefficient p characterizing the contact ratio dA_r/dA_n and controlling the normal shear distribution (Eq. (27)). Table 3 summarizes the cutting conditions and the experimental average friction coefficient $\overline{\mu}$ obtained from the ratio of the mean cutting forces F_p^{exp} and F_q^{exp} (Eq. (20)).

Table 3 Orthogonal machining conditions and numerical results for different cutting speeds V, uncut chip thicknesses t_2 and tool rake face angles α. The average friction coefficient $\overline{\mu}$ represents the average of cutting forces acting on the tool-chip interface

	$\overline{\mu}$	V	f	α	L_c	$\frac{L_s}{L_c}$	p	t_2	ϕ	σ_0	$\overline{\tau}_{st}$	T_{max}	F_p^{num}	F_q^{num}	F_p^{exp}	F_q^{exp}
TiAlN	0.82	15	0.12	20	0.262	1	0.34	0.20	35	897	565	686	881	309	750	260
	0.8	30	0.12	20	0.266	1	0.37	0.20	35	908	552	803	890	300	750	250
	1	60	0.12	20	0.364	1	0.74	0.21	32.5	872	500	964	933	435	600	280
	0.86	60	0.2	5	0.884	1	1.44	0.4	27	1220	428	1061	1885	1354	–	–
	0.98	60	0.2	15	0.808	1	1.37	0.38	30	1051	435	1024	1749	986	–	–
	1	60	0.2	30	0.506	1	0.74	0.32	37.5	820	470	976	1299	348	–	–
WC-Co	1	60	0.2	5	1.3	1	2.37	0.44	25	1203	356	1199	2005	1682	–	–
	1	60	0.2	15	0.9	1	1.68	0.38	30	1040	388	1153	1710	987	–	–
	1	60	0.2	30	0.576	1	1.13	0.32	37.5	878	433	1071	1362	365	–	–

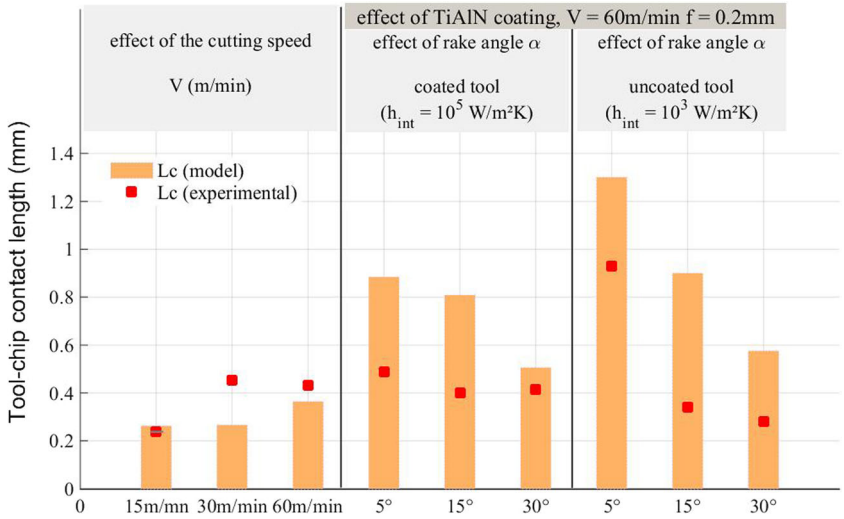

Fig. 11 Effect of the cutting speed V of the rake face angle and the heat conductance on the tool–chip contact length

5 Discussions

The numerical results include the tool-chip contact length L_c, the ratio of the sticking zone, the chip thickness t_2, the shear angle ϕ, the maximum normal stress at the tool tip σ_0, the average shear stress $\overline{\tau}_{st}$ at the TCI, the maximum tool-chip interface temperature $T_{\max}$ and contact forces F_N and F_f (Eq. (21)).

Combining Eq. (20) and Eq. (25), the cutting force F_p^{num} and the feed force F_q^{num} can be deduced:

$$F_p^{\text{num}} = \left(\frac{1 + \overline{\mu}\cdot\tan\alpha}{1 + \tan\alpha^2}\right)\frac{L_c\cdot\overline{\tau}_{st}\cdot w}{\overline{\mu}\cdot\cos\alpha} \tag{35}$$

$$F_q^{\text{num}} = \left(\frac{\overline{\mu} - \tan\alpha}{1 + \tan\alpha^2}\right)\frac{L_c\cdot\overline{\tau}_{st}\cdot w}{\overline{\mu}\cdot\cos\alpha} \tag{36}$$

The tool–chip contact lengths and cutting forces reported respectively, in Figs. 11 and 12, are in good agreement with the experimental tendencies.

5.1 Thermal aspects of the contact

As shown Table 3, the high level of the average friction coefficient ($\overline{\mu}\approx 1$) can be considered as a good indicator of adhered friction mode with fully sticking contact at the TCI ($L_s/L_c=1$). Numerical results showing a sticking contact on overall the TCI are in good agreement with experimental observations presented in Fig. 4. An adhesive layer is clearly noticeable, even at the end of the contact. These results differ from traditional approaches which are commonly referred to Zorev's model [15], where the existence of a sliding contact at the end of contact is assumed. The assumption of sliding is generally argued by the presence of low pressure in this region of contact. However, for friction of titanium, it was already observed that a sticking regime is possible under low pressure such as in the work of Gras and Courtell [45]. In their experiments, the normal load is varied from 0 to 500 N applied on than apparent contact surface of 2.2 cm^2, and the sliding velocity is varied from 0 to 1.75 m/s. The authors have been studied the effect of temperature on the friction of titanium

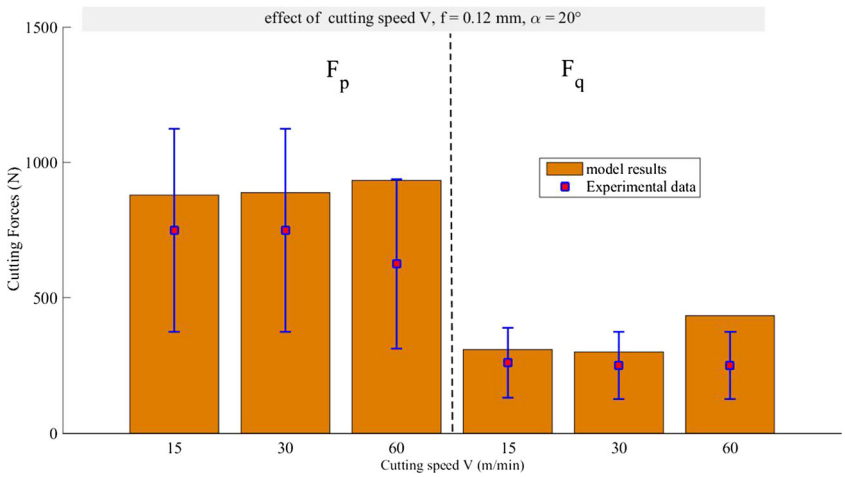

Fig. 12 Effect of the cutting speed V on the cutting force and on the feed force

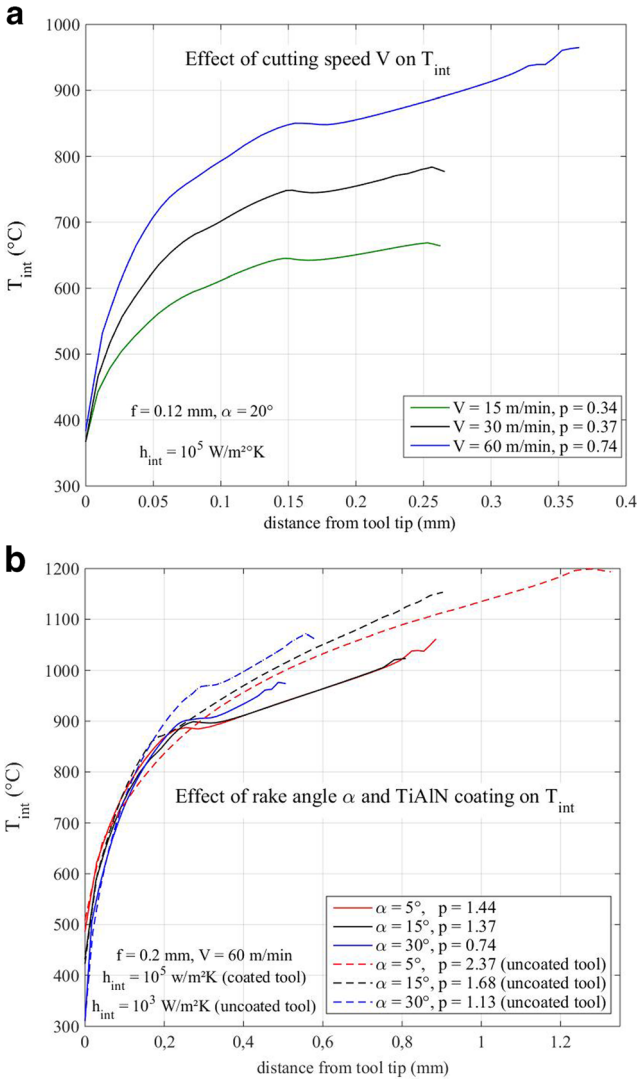

Fig. 13 **a** Effect of the cutting speed V on the temperature distribution. **b** Effect of the rake face angle and the heat conductance on the temperature distribution at the TCI

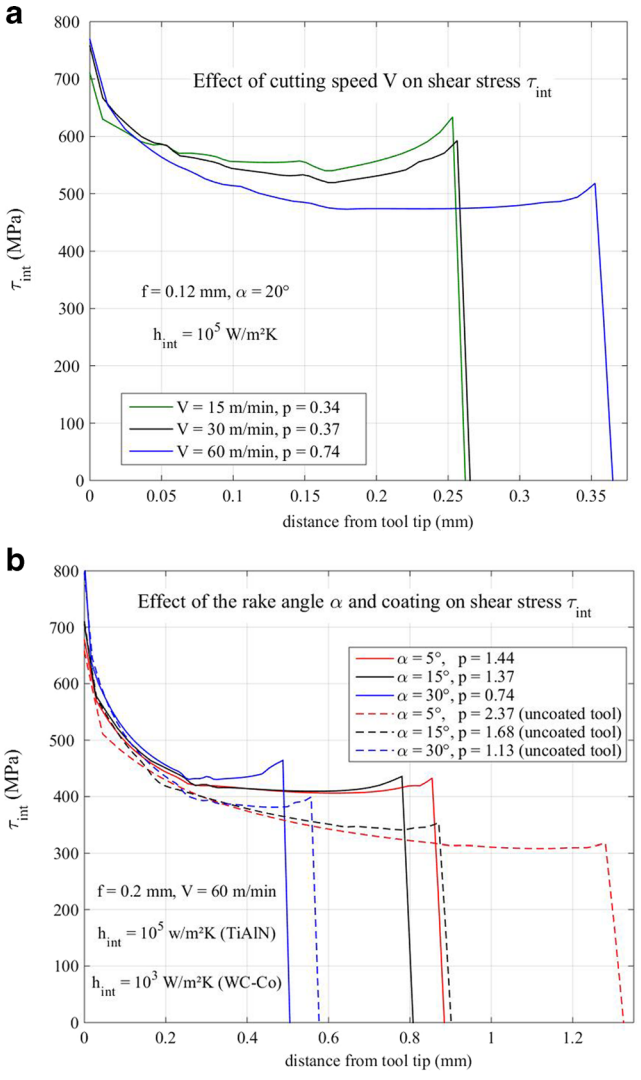

Fig. 14 **a** Effect of the cutting speed V on the shear stress distribution. **b** Effect of the rake face angle and the heat conductance on the shear stress distribution at the TCI

and titanium alloy Ti6Al4V and have shown that around a critical temperature of about 300 °C, the contact is characterized by high friction and evident surface wear due to the interpenetration of the materials in contact by the combined action of high temperature and stress which simultaneously weaken the subsurface layers and favor adhesion. When temperature is around 600 °C, fully seizure occurs with melt bonds along the friction contact, shearing occurs within the subsurface heaving the slightest strength. The average friction coefficient grows from $\overline{\mu} = 1$ at 300 °C to $\overline{\mu} = 4$ at 700 °C. Similar thermal conditions are also present at the TCI during cutting of titanium, and the temperature appears to be the most determining factor favoring a regime of sticking contact (see Fig. 13). The heat conductance h_{int} also influences the heat partition on the tool–chip interface; an increase of this parameter implies a growth of the heat transfer towards the tool side. As shown in Fig. 13, the increase of the heat conductance increases the dissipation of the heat on the interface and reduces the thermal softening within the SSZ as shown in the case of TiAlN-coated tool. However, in the case of the WC-Co uncoated tool, the heat conductance is 100 less than in the previous case. Consequently, the thermal softening is more important due to reduced thermal dissipation effect on the TCI. It leads also to the increase of the tool–chip contact length and cutting forces. In Fig. 13a, the effect of the cutting speed is illustrated in the case of the TiAlN-coated tool. The increase of the cutting speeds increases the strain rate and mainly the heat flux in the SSZ, Eq. (30)), and by consequence the temperature.

5.2 Distribution of stresses at the TCI

As said before, a fully sticking contact is observed for all the cases. However, the results of the simulations show that the

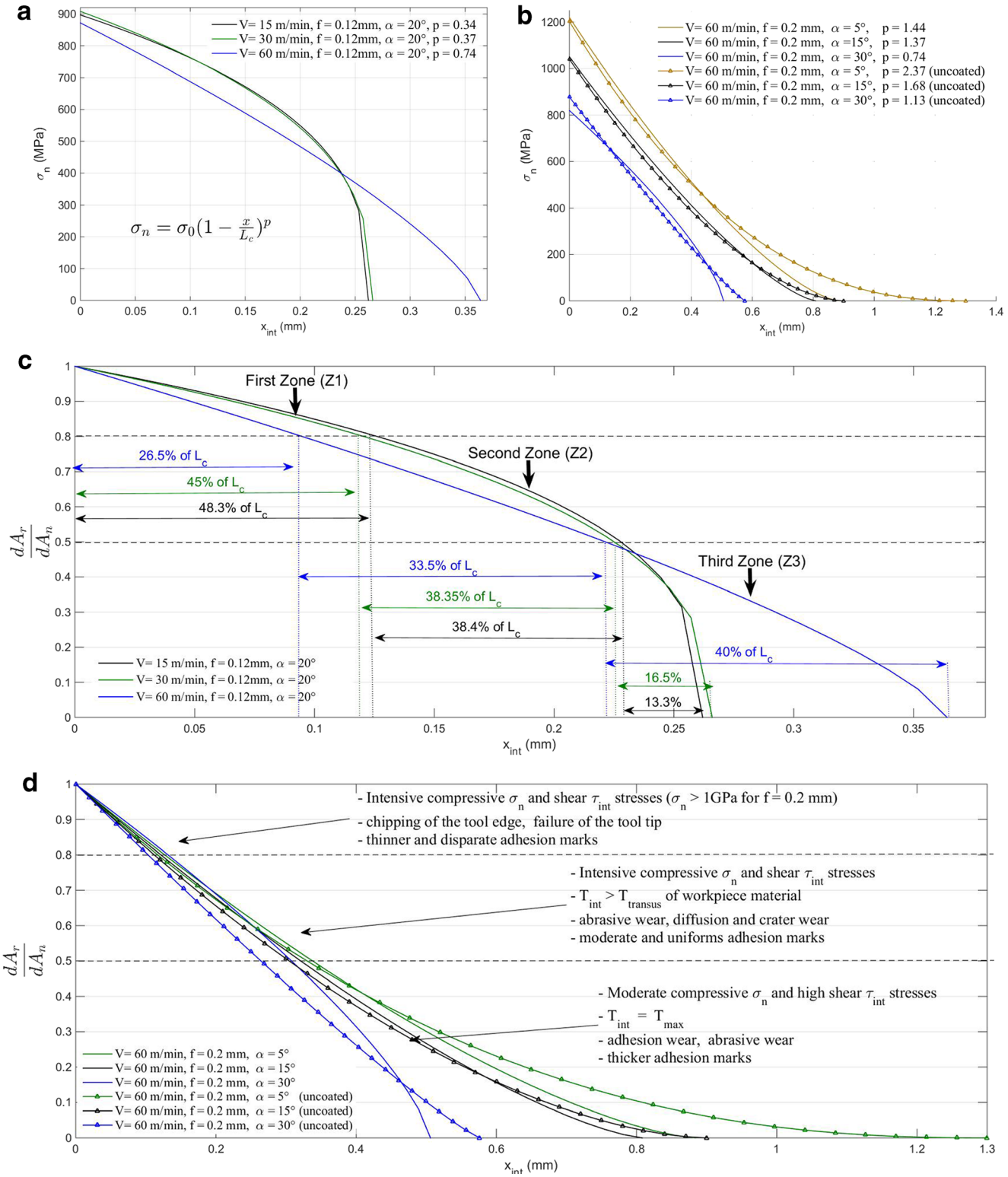

Fig. 15 **a** Predicted normal loading at the TCI for TiAlN-coated tool and f=0.12 mm. **b** Predicted normal loading at the TCI for different rake angle, (V=60 m/min, f=0.2 mm). **c** Repartition of the ratio along the TCI for TiAlN-coated tool and f=0.12 mm. **d** Repartition of the ratio along the TCI for different rake angle (V=60 m/min, f=0.2 mm) and suggested wear mechanisms correlated with numerical distributions of temperature and stresses

distribution of shear and normal stresses at the TCI may be very different (see Figs. 14 and 15). Equations (15) and (16) allow the model to establish a link between the distribution of the normal stress and the ratio dA_r/dA_n with the parameter p. This coefficient also controls the tool–chip contact length L_c as highlighted in Eq. (19). Although the cutting speed V does not seem to have a significant effect on the average of the shear stress and on the maximum normal stress located at the tool tip, (Figs. 14a and 15a), the increase of V leads to increase of the coefficient p. For the high coefficients p, normal pressure is more concentrated at the tool tip and then decreases rapidly until the contact length. In this case, the major part of contact have a ratio $dA_r/dA_n < 0.5$ favoring the oxygen penetration, see Fig. 15d for V=60 m/min and f=0.2mm, and also Fig. 4. Moreover, at some distance from the tool-tip, the combined effect of the high shear stress ($\tau_{int} \geq 400$ MPa), of the moderate normal stress (200 MPa $\leq \sigma_n \leq$ 400 MPa) and of the high temperature, favorite adhesion and abrasive wear as shown on Fig. 3b–d. At the lower cutting speed, the coefficient p tends to decrease, leading to a smaller contact length with a more homogenous repartition of the normal load σ_n along the main part of the contact, as shown by Figs. 14 and 15. Adhesion marks are thin and disparate because the major part of the contact has a ratio dA_r/dA_n close to the unity, thus limiting the penetration of oxygen into the contact especially close to the tool tip (see also Fig. 3). From a point of view of wear, this can be considered as an indicator of the apparition of the built-up layer mechanism, according to experimental tendencies shown by Trent and Wright [17]. In addition to the effect of high temperature, the level of the coefficient p can also inform about adhesion rate on the TCI.

As said in the Section 1, the two common approaches to measuring normal and frictional stress distributions on the tool rake face are the split-tool and photo elastic method. Although the first technique was criticized for not having adequate resolution in the vicinity of the cutting edge, a necessity to have a split tool-material stronger then Ti6Al4V and not appropriated for smaller tool–chip contact length. The second technique is not possible to use to characterize the stress distributions because the photoelastic materials, used as cutting tool, have a limited strength and applied to very low cutting speed (mm/min).

The rake angle has also an influence on the stress distribution. The increase of this angle leads to the increase of the shear angle ϕ characterizing the inclination of the primary shear zone, (see Zvorykin's law, Eq. (34)). This induces a decrease of the saturated strain γ_h, the decrease of shear stress on the PSZ and leads to a decrease of the normal stress at the tool tip σ_0 (see Eq. (11) and Eq. (18)). However, the increases of the feed f and the rake angle α shift the major part of the compressive stress σ_n toward the tool tip (see Fig. 13). This trend is also confirmed by the micrographs in Fig. 4, where the delamination and the notching of the tool substrate are more concentrated close to the tool tip. This fact is due to the reduction of the coefficient p with the respect of the increase of the rake face angle. Remind that the average friction coefficient $\overline{\mu}$ is quasi constant for different rake angle.

6 Conclusion

The modeling of the thermomecanical mechanisms at the tool chip interface (TCI) was applied to investigate the friction phenomenon at the secondary shear zone (SSZ). Based on a hybrid model approach for metal cutting, new results and discussions were supported by (1) the application of a new velocity field with a non linear profile to describe the material flow at the SSZ and (2) the introduction of the evolution of the ratio A_r/A_n between the real and apparent contact area along the TCI. The model was employed to study the case of dry machining of a Ti6Al4V alloy with coated and uncoated tools. The model is able to predict different contacts regimes such as the perfectly sliding contact (sliding mode), the sticking-sliding contact (transition mode) and the fully sticking contact (adhered friction mode). In the case of the Ti6Al4V, the last (fully sticking) appears as the main regime occurred along the TCI. The adhered friction describes the chip flow by shearing within secondary shear zone and reproduces the non-sliding velocity overall the TCI. In this case, the singularity of the fully sticking contact allowed the model to completely solve the problem of chip formation including not only the estimation of the cutting forces and cutting temperature but also the tool–chip contact length L_c, the repartition of the real area A_r, which transmits the rake face forces, with regard to the apparent area A_n and the evolution of the normal and shear stress along the TCI. It was shown, that in the first part of contact, the ratio between the real and apparent contact area A_r/A_n is tending to 1, so limiting the formation of thicker adhesion marks but favorites chipping, notching and failure of the tool tip due to the influence of high stresses. At a certain distance from the tool tip, when the ratio decreases ($0.5 \leq A_r/A_n \leq 0.8$), the combined effect of the heating, due to the plastic deformation in the SSZ, and of the moderate stresses favorites three wear mechanisms: (i) weakening and delamination of TiAlN coating, (ii) moderate adhesion marks due to the presence of oxygen on the TCI and (iii) diffusion wear and abrasion due to the separated particles. Finally, at the end of contact, the temperature reaches a maximum level, the stresses reach their minimum levels and the ratio A_r/A_n tends to zero. These conditions favor the presence of oxygen in the vacua between asperities and then lead to a thicker adhesion layer. The effects of the cutting speed and of the tool rake face angle are also simulated to be confronted qualitatively with experimental observations. The more is the cutting velocity important, the higher is the contact length and inversely with the rake angle. This repartition was correlated with the spread adhesion marks

printed on the worn tool rake faces and with the numerical distributions of the temperature, shear and normal stresses. According to the heat exchange at the TCI, the presence of the titanium into the TiAlN coating is considered as favoring the adhered friction and heat conductance. The increase of the conductance tends to reduce the tool–chip contact length, to decrease the thermal softening on the SSZ, to reduce the temperature and leads to homogenize the repartition of the normal stress at the TCI.

References

1. Usui E, Shirakashi T (1982) Mechanics of machining—from "descriptive" to "predictive" theory, on the art of cutting metals—75 years later. ASME PE 7:13–35
2. Childs THC, Mahdi MI, Barrow G (1989) On the stress distribution between the chip and tool during metal turning. CIRP Ann Manuf Technol 38:55–58
3. Kato S, Yamaguchi K, Yamada M (1972) Stress distribution at the interface between tool and chip in machining. J Manuf Sci Eng 94: 683–689
4. Bagchi A, Wright PK (1987) Stress analysis in machining with the use of sapphire tools. Proc R Soc Lond A Math Phys Sci 409:99–113
5. Amini E (1968) Photoelastic analysis of stresses and forces in steady cutting. J Strain Anal Eng Des 3:206–213
6. Usui E, Takeyama H (1960) A photoelastic analysis of machining stresses. J Manuf Sci Eng 82:303–307
7. Sutter G, Ranc N (2007) Temperature fields in a chip during high-speed orthogonal cutting—an experimental investigation. Int J Mach Tools Manuf 47:1507–1517
8. M'saoubi R, Lebrun JL, Changeux B (1998) A new method for cutting tool temperature measurement using CCD infrared technique: influence of tool and coating. Mach Sci Technol 2: 369–382
9. Battaglia J-L, Cois O, Puigsegur L, Oustaloup A (2001) Solving an inverse heat conduction problem using a non-integer identified model. Int J Heat Mass Transf 44:2671–2680
10. Trent EM (1988) Metal cutting and the tribology of seizure: III temperatures in metal cutting. Wear 128:65–81
11. Merchant ME (1945) Mechanics of the metal cutting process. I. Orthogonal cutting and a type 2 chip. J Appl Phys 16:267–275
12. Merchant ME (1945) Mechanics of the metal cutting process. II. Plasticity conditions in orthogonal cutting. J Appl Phys 16: 318–324
13. Astakhov VP (2006) Tribology of metal cutting, Elsevier
14. Oxley PLB (1989) The mechanics of machining: an analytical approach to assessing machinability, E. Horwood
15. Zorev NN (1966) Metal cutting mechanics, Pergamon Press
16. Trent EM (1988) Metal cutting and the tribology of seizure: I seizure in metal cutting. Wear 128:29–45
17. Trent EM, Wright PK (2000) Metal cutting, Butterworth-Heinemann
18. Wright PK, Horne JG, Tabor D (1979) Boundary conditions at the chip-tool interface in machining: comparisons between seizure and sliding friction. Wear 54:371–390
19. El Mansori M, Mkaddem A (2007) Surface plastic deformation in dry cutting at magnetically assisted machining. Surf Coat Technol 202:1118–1122. doi:10.1016/j.surfcoat.2007.07.104
20. Molinari A, Cheriguene R, Miguélez H (2011) Numerical and analytical modeling of orthogonal cutting: the link between local variables and global contact characteristics. Int J Mech Sci 53:183–206
21. Marinov VR (2001) Hybrid analytical–numerical solution for the shear angle in orthogonal metal cutting—part I: theoretical foundation. Int J Mech Sci 43:399–414
22. Marinov VR (2001) Hybrid analytical–numerical solution for the shear angle in orthogonal metal cutting—part II: experimental verification. Int J Mech Sci 43:415–426
23. S. Bahi, Modélisation hybride du frottement local à l'interface outil-copeau en usinage des alliages métalliques. Ph.D. Thesis (in french). https://pastel.archives-ouvertes.fr/pastel-00602396.
24. Bahi S, Nouari M, Moufki A, Mansori ME, Molinari A (2012) Hybrid modelling of sliding–sticking zones at the tool–chip interface under dry machining and tool wear analysis. Wear 286:45–54
25. Bahi S, Nouari M, Moufki A, El Mansori M, Molinari A (2011) A new friction law for sticking and sliding contacts in machining. Tribol Int 44:764–771
26. Bowden FP, Tabor D (1939) The area of contact between stationary and between moving surfaces, in: Proc R Soc Lond A Math Phys Sci. pp. 391–413
27. Childs THC, Maekawa K, Obikawa T, Yamane Y (2000) Metal Machining: Theory and Applications, Butterworth-Heinemann
28. Gerth J, Gustavsson F, Collin M, Andersson G, Nordh L-G, Heinrichs J et al (2014) Adhesion phenomena in the secondary shear zone in turning of austenitic stainless steel and carbon steel. J Mater Process Technol 214:1467–1481
29. Childs THC (2006) Friction modelling in metal cutting. Wear 260: 310–318
30. Finnie I, Shaw MC (1956) The friction process in metal cutting. Trans ASME 78:1649
31. Sutter G, List G (2013) Very high speed cutting of Ti6Al4V titanium alloy—change in morphology and mechanism of chip formation. Int J Mach Tools Manuf 66:37–63
32. Arnoux J-J, Sutter G, List G (2012) Characterization of Dynamic Friction Factor for FEM Modeling of High Speed Process
33. Qi HS, Mills B (2000) Formation of a transfer layer at the tool-chip interface during machining. Wear 245:136–147
34. M'Saoubi R, Chandrasekaran H (2005) Innovative methods for the investigation of tool-chip adhesion and layer formation during machining. CIRP Ann Manuf Technol 54:59–62
35. Wiklund U, Rubino S, Kádas K, Skorodumova NV, Eriksson O, Hedberg S et al (2011) Experimental and theoretical studies on stainless steel transfer onto a TiN-coated cutting tool. Acta Mater 59:68–74
36. Oxley PLB, Hastings WF (1976) Minimum work as a possible criterion for determining the frictional conditions at the tool/chip interface in machining. Philos Trans R Soc London Ser Math Phys Sci 282:565–584
37. Bao H, Stevenson MG (1976) An investigation of built-up edge formation in the machining of aluminium. Int J Mach Tool Des Res 16:165–178
38. Dudzinski D, Molinari A (1997) A modelling of cutting for viscoplastic materials. Int J Mech Sci 39:369–389
39. Johnson GR, Cook WH (1983) A constitutive model and data for metals subjected to large strains, high strain rates and high temperatures, in: Proc. 7th Int. Symp. Ballist. pp. 541–547

40. Moufki A, Molinari A, Dudzinski D (1998) Modelling of orthogonal cutting with a temperature dependent friction law. J Mech Phys Solids 46:2103–2138
41. Lim SC, Ashby MF (1987) Overview no. 55 wear-mechanism maps. Acta Metall 35:1–24
42. Grzesik W, Nieslony P (2003) A computational approach to evaluate temperature and heat partition in machining with multilayer coated tools. Int J Mach Tools Manuf 43:1311–1317
43. Boivineau M, Cagran C, Doytier D, Eyraud V, Nadal M-H, Wilthan B (2006) Propriétés thermophysiques de l'alliage Ti6Al4V (TA6V) à l'état solide et liquide. Int J Thermophys 27(2):507–529
44. Zvorykin KA (1893) Work and stress necessary for separation of metal chips. Proc. Kharkov Technol. Inst, Ukr
45. Gras R, Courtel R (1973) Frottement à haute température du titane et de l'alliage TA6V. Wear 26:1–26